Journal of Catalysis 407 (2022) 141–148

Contents lists available at ScienceDirect

Journal of Catalysis

journal homepage: www.elsevier.com/locate/jcat

Bimetallic M_xRu_{100-x} nanoparticles (M = Fe, Co) on supported ionic liquid phases (M_xRu_{100-x}@SILP) as hydrogenation catalysts: Influence of M and M:Ru ratio on activity and selectivity

Sheetal Sisodiya-Amrute [a], Casey Van Stappen [a], Simon Rengshausen [a], Chenhui Han [a], Alexandre Sodreau [a], Claudia Weidenthaler [c], Simon Tricard [d], Serena DeBeer [a], Bruno Chaudret [d], Alexis Bordet [a,*], Walter Leitner [a,b,*]

[a] Max Planck Institute for Chemical Energy Conversion, Stiftstraße 34-36, 45470 Mülheim an der Ruhr, Germany
[b] Institut für Technische und Makromolekulare Chemie RWTH, Aachen University, 52074 Aachen, Germany
[c] Max-Planck-Institut für Kohlenforschung, Kaiser-Wilhelm-Platz 1, 45470 Mülheim an der Ruhr, Germany
[d] Laboratoire de Physique et Chimie des Nano-Objets, Université de Toulouse, LPCNO, INSA, UPS, CNRS-UMR5215, 135 Avenue de Rangueil, 31077 Toulouse, France

ARTICLE INFO

Article history:
Received 15 November 2021
Revised 6 January 2022
Accepted 31 January 2022
Available online 4 February 2022

Keywords:
Bimetallic nanoparticles
SILP
Ruthenium
Iron
Cobalt
Catalytic hydrogenation
Synergistic effect

ABSTRACT

Bimetallic iron-ruthenium and cobalt-ruthenium nanoparticles with systematic variations in the Fe:Ru and Co:Ru ratios are prepared following an organometallic approach and immobilized on an imidazolium-based supported ionic liquid phase (SILP). Resulting M_xRu_{100-x}@SILP materials are characterized by electron microscopy, X-ray diffraction and X-ray absorption spectroscopy, confirming the formation of small, well-dispersed and alloyed zero-valent bimetallic nanoparticles. A systematic comparison of the performances of Fe_xRu_{100-x}@SILP and Co_xRu_{100-x}@SILP catalysts is made using the hydrogenation of benzilideneacetone as model reaction. The M:Ru ratio is found to have a critical influence on activity and selectivity, with clear synergistic effects arising from the combination of the noble and 3d metals. Co_xRu_{100-x}@SILP catalysts are significantly more reactive to reach a given selectivity at a systematically higher content of the 3d metal as compared to the Fe_xRu_{100-x}@SILP catalysts, evidencing a remarkable influence of the nature of the "diluting" 3d metal on the overall performance of the M_xRu_{100-x}@SILP catalysts.

1. Introduction

Selective catalytic hydrogenation is one of the fundamental pillars of the chemical industry, and is essential not only for the production of fine chemicals and pharmaceuticals, but also for the conversion of renewable feedstocks to value-added chemicals [1,2]. In metal nanoparticle-catalyzed hydrogenation reactions, the observed selectivity and activity are intimately linked to the efficiency and mode of activation of both molecular hydrogen (H_2) and the substrate [1–5]. In particular, the hydrogenation of C=C bonds in alkenes and arenes is known to be facilitated by the homolytic cleavage of H_2 to give H-H (*i.e.* non-polarized activation). In contrast, the reduction of C=O bonds is typically favored by the heterolytic cleavage of H_2 to give $H^{\delta+}$-$H^{\delta-}$ (*i.e.* polarized H_2 activation). Similarly, unsaturated functional groups in substrates may be more or less easy to reduce depending on the ability of the metal(s) considered to activate them. For example, the hydrogenation of aromatic rings is typically favored on surfaces displaying arrangements of 3–4 noble metal atoms (ex. Ru, Rh).[6] Meanwhile, the activation of polar functionalities such as C=O bonds in aldehydes or ketones are facilitated on more oxophilic surfaces [2,3]. Thus, achieving the efficient and selective reduction of targeted unsaturated moieties in multifunctional substrates requires precise control of the interplay between activation of H_2 and substrate. In this context, several methods have been developed through the years, including, for example, the use of ligands [7–9], the selective poisoning of NPs surface [10–12], the synthesis of nanoparticles of different sizes [13,14], etc. Recently, the combination of metals to produce bimetallic core–shell or alloyed nanostructures has also attracted significant attention to tune the reactivity of nanoparticle catalysts [5,15–17]. The combination of noble metals with first row base metals is a particularly promising

* Corresponding authors at: Max Planck Institute for Chemical Energy Conversion, Stiftstraße 34-36, 45470 Mülheim an der Ruhr, Germany (A. Bordet, W. Leitner).
E-mail addresses: alexis.bordet@cec.mpg.de (A. Bordet), walter.leitner@cec.mpg.de (W. Leitner).

https://doi.org/10.1016/j.jcat.2022.01.030
0021-9517/

strategy in this respect, and was shown to unlock activities, selectivities and synergistic effects that have thus far not been possible for the metals taken individually [5,15–17]. However, while crucial for the preparation of high quality supported bimetallic NPs with tunable metal ratios, the development of appropriate and versatile synthetic approaches and supporting matrices remains challenging [18,19]. In this context, our group has recently shown that bimetallic FeRu and CoRh nanoparticles can be easily prepared in imidazolium-based supported ionic liquid phases (SILP) and applied to selective hydrogenation and hydrogenolysis reactions [20–23]. Interestingly, metal ratios were found to dictate the activity and selectivity of Fe_xRu_{100-x}@SILP and Co_xRh_{100-x}@SILP catalysts, and especially their ability to hydrogenate aromatic rings in substrates containing C=C, C=O bonds and aromatics [23]. However, achieving a precise control of the selectivity and activity of hydrogenation catalysts still remains a major objective and challenge. In addition, systematic studies investigating the influence of the nature of the metals and the metal ratios on the hydrogenation performances of bimetallic catalysts are scarce, however, such studies are essential to enable knowledge-based catalytic design.

In this context, we have set our goal to systematically study bimetallic nanoparticles composed of Ru in combination with Fe and Co and immobilized within an imidazolium-based SILP matrix. The application of bimetallic FeRu NPs (supported or not) in catalysis has been well studied in the past decade, especially for hydrogenation and hydrodeoxygenation reactions [20–22,24–26]. In contrast, CoRu NPs have been mostly used in electrochemistry [27–29] and for transformations such as hydrogen generation from ammonia borane [30] and dimethamine-borane [31], but were rarely explored in hydrogenation [32–33]. In addition, there is, to the best of our knowledge, no systematic comparison of the hydrogenation performances of bimetallic FeRu and CoRu nanoparticles. Herein, we present the preparation of a series of bimetallic Fe_xRu_{100-x}@SILP and Co_xRu_{100-x}@SILP catalysts with varying metal ratios following an organometallic approach. This involves the co-reduction of the metal precursors $\{Fe[N(Si(CH_3)_3)_2]_2\}_2$ or [Co(cod)(cyclooctadienyl)] with [Ru(cod)(cot)] (cod = 1,5 cyclooctadiene and cot = 1,3,5 cyclooctatriene) in the presence of a SILP produced through the covalent grafting of imidazolium-based ionic liquids on dehydroxylated silica (Fig. 1a). The comparable stability during handling and ligand lability upon hydrogenation of the chosen [Fe], [Co] and [Ru] organometallic precursors are the key to produce bimetallic Fe_xRu_{100-x} and Co_xRu_{100-x} of similar physicochemical properties and tunable composition. The resulting Fe_xRu_{100-x}@SILP and Co_xRu_{100-x}@SILP materials were characterized using a combination of techniques including electron microscopy, XRD, and XAS to determine the NPs size, dispersion, oxidation state and alloying properties (Fig. 1b). The influence of the nature of the 3d metal used as well as of the M:Ru ratios (M = Fe, Co) on the hydrogenation performances (activity, selectivity) of M_xRu_{100-x}@SILP catalysts was systematically investigated using benzylideneacetone as a molecular probe and prototypical example for substrates with several potentially reducible moieties (Fig. 1c).

2. Results and discussion

2.1. Synthesis

The imidazolium-based supported ionic liquid phase (SILP) was synthesized following a previously published procedure [20]. This involved the condensation of the triethoxysilane functionalized ionic liquid [1-butyl-3-(3-triethoxysilylpropyl)-imidazolium]NTf_2 with dehydroxylated SiO_2. This SILP structure was selected for its proven ability to facilitate the formation and stabilization of mono- and bimetallic nanoparticles [14,20–23]. Bimetallic M_xRu_{100-x}@SILP (M = Fe, Co) catalysts with systematically varied M:Ru ratios were synthesized by adapting an organometallic synthetic approach developed in our group for the preparation of $Fe_{25}Ru_{75}$@SILP [20]. For that, the metal precursors $\{Fe[N(Si(CH_3)_3)_2]_2\}_2$ or [Co(cod)(cyclooctadienyl)] and [Ru(cod)(cot)] were reduced *in situ* in the presence of the SILP under an atmosphere of H_2 (3 bar) at 150 °C with mesitylene as a solvent (total metal loading = 1 mol%).

2.2. Characterization

BET measurements showed that the Fe_xRu_{100-x}@SILP and Co_xRu_{100-x}@SILP materials possess a surface area of about 285 $m^2 \cdot g^{-1}$. As expected, this surface area is lower than for the starting dehydroxylated silica (343 $m^2 \cdot g^{-1}$) due to the presence of the chemisorbed ionic liquid. The theoretical total metal loading

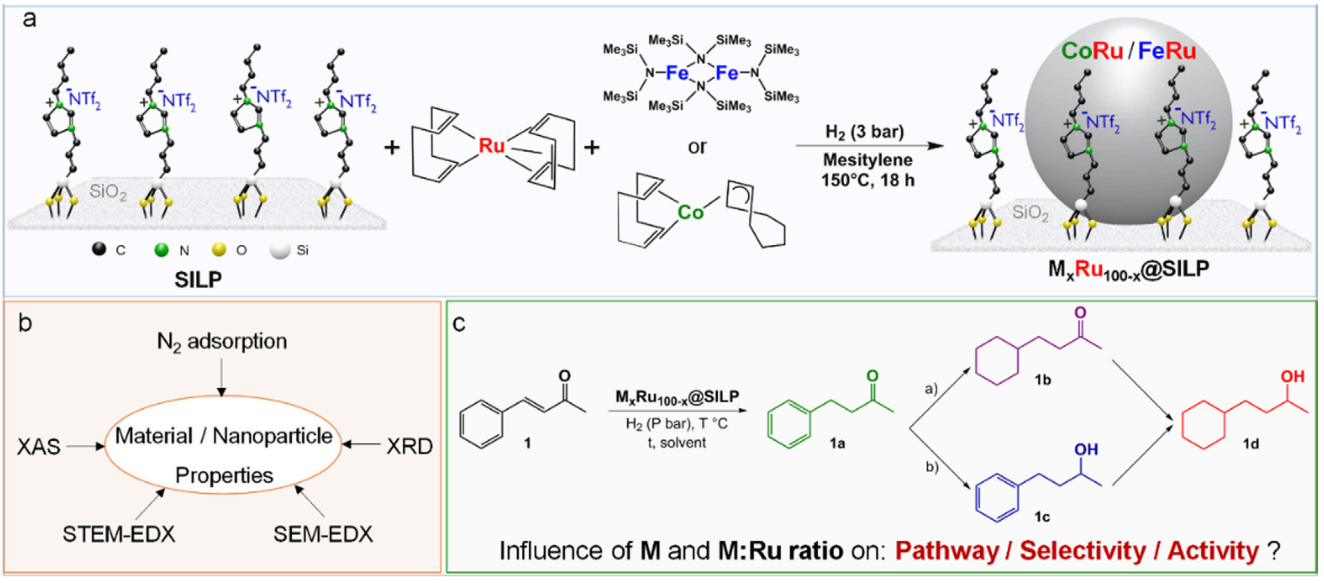

Fig. 1. Methodology followed in this study. (a) Organometallic synthesis, (b) characterization, and (c) evaluation of the catalytic performances of M_xRu_{100-x}@SILP (M = Fe, Co) catalysts.

and M:Ru ratios were confirmed by scanning electron microscopy with energy dispersive X-ray spectroscopy (SEM-EDX) (for details see Tables S1 and S2 in the Supporting Information). Characterization of the Fe_xRu_{100-x}@SILP and Co_xRu_{100-x}@SILP materials by transmission and scanning transmission electron microscopy (STEM) evidenced the formation of small (1.5–4 nm) and well-dispersed NPs on the SILP ($Fe_{25}Ru_{75}$@SILP and $Co_{50}Ru_{50}$@SILP are given as example in Fig. 2, additional details are given in Tables S1, S2 and Figs. S1–S9 in the Supporting Information). No clear trend linking the NPs size and the nature of the 3d metal or the M:Ru ratio was identified. Elemental mapping using STEM-HAADF-EDX (HAADF = high angle annular dark field) confirmed the formation of NPs containing both Fe and Ru as well as Co and Ru, as exemplified for $Fe_{25}Ru_{75}$@SILP in Fig. 2b-c and $Co_{50}Ru_{50}$@SILP in Fig. 2e-f (see Figs. S10 and S11 in the Supporting Information for other examples). Overall, these data confirm the versatility of the organometallic approach in the controlled formation of bimetallic NPs on SILP.

The properties of $Fe_{25}Ru_{75}$@SILP were previously studied by metal K-edge and EXAFS, evidencing zero-valent Fe and Ru atoms organized in a bimetallic structure [20]. We have further characterized the oxidation state and alloying properties of Co_xRu_{100-x}@SILP materials presently by performing X-ray absorption spectroscopy (XAS) on a series of materials with x = 0, 20, 30, 50, 75, and 100. Full details regarding data collection, processing, and analysis can be found in the SI.

The Co K-edge XAS spectra (Fig. 3a) of Co_{100}@SILP generally resembles that of metallic Co, presenting a pre-edge shoulder at ~7712 eV, and a rising edge spanning from ~7715–7722 eV (centered at ~7719 eV). This is consistent with our previous observations for Co_{100}@SILP, and supports a zero-valent Co oxidation state in the bulk [23]. For comparison, the spectrum of O_2-exposed Co_{100}@SILP is presented in the SI to provide a gauge of bulk oxidation state, where a decrease in pre-edge intensity is accompanied by a large increase in white-line intensity (Figs. S12–S13). Upon addition of 20–30% Ru to form $Co_{80}Ru_{20}$@SILP and $Co_{70}Ru_{30}$@SILP, the pre-edge shoulder becomes less well-defined, and the rising edge shifts approximately 1 eV to lower energy (relative to Co_{100}@SILP). This shift in rising edge indicates a decrease in the relative energy of the Co 4p shell, and may indicate a change in average local symmetry of Co modulated by

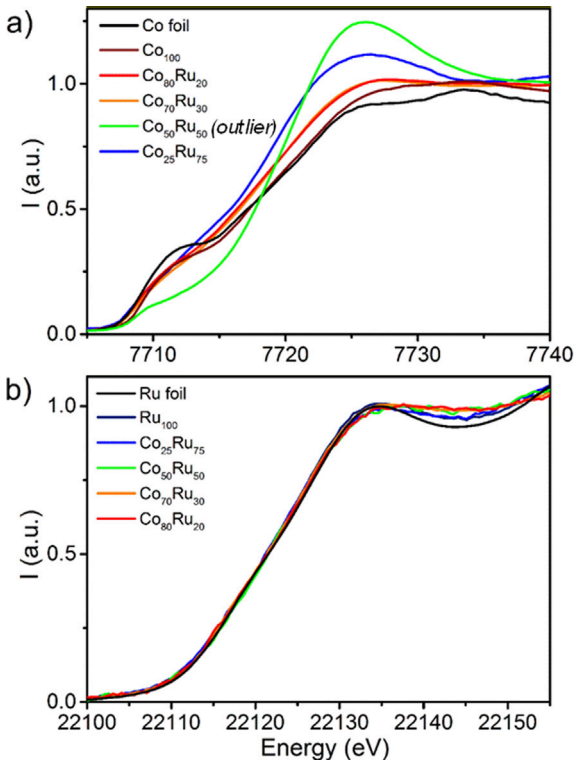

Fig. 3. Comparison of normalized (a) Co K-edge and (b) Ru K-edge XAS for Co_x-Ru_{100-x}@SILP, x = 100, 80, 70, 50, 25, and 0.

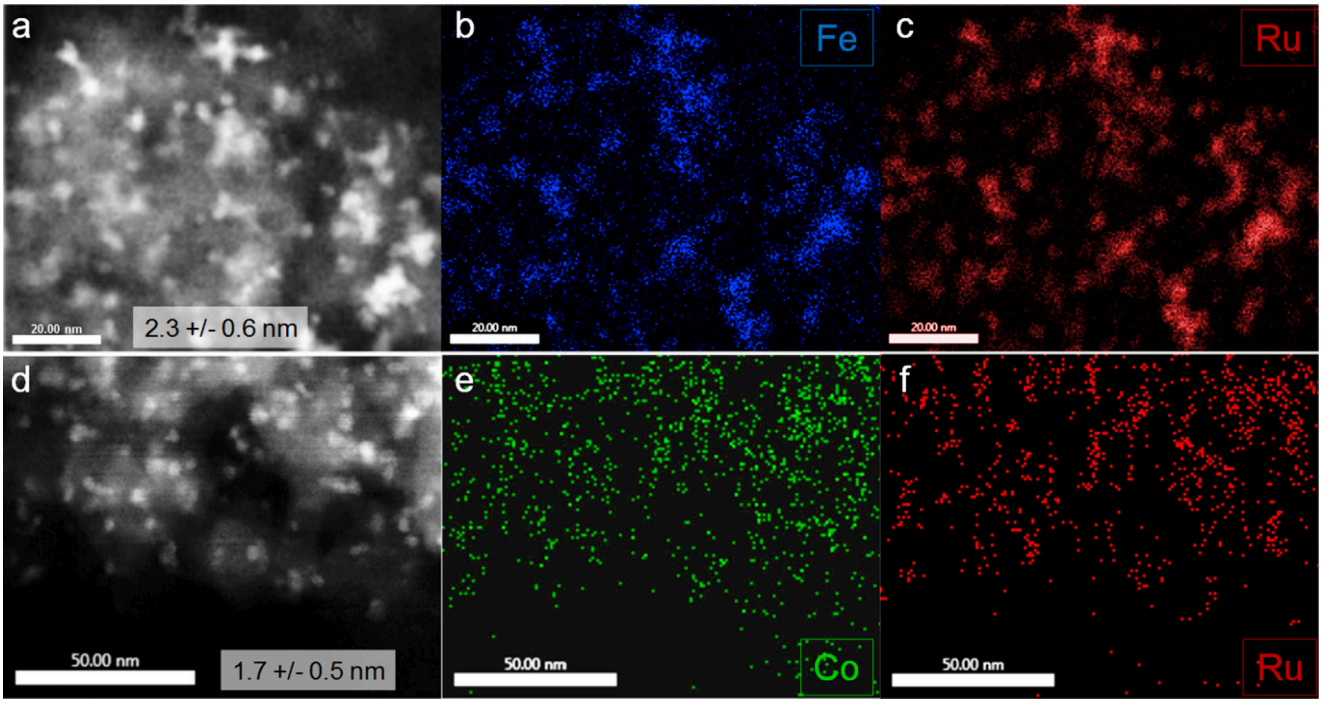

Fig. 2. STEM-HAADF images of: (a) $Fe_{25}Ru_{75}$@SILP with (b) elemental mapping of Fe K, (c) elemental mapping of Ru L; and (d) $Co_{50}Ru_{50}$@SILP with (e) elemental mapping of Co K, (f) elemental mapping of Ru L.

the presence of Ru. Additionally, a small increase in white-line intensity ~7726 eV is observed. The white-line is a generally ill-defined region arising from a combination of both excitations to higher valence-bound states as well as low kinetic-energy scattering phenomena. Addition of more Ru to form $Co_{25}Ru_{75}$@SILP further exacerbates the changes observed for $Co_{80}Ru_{20}$@SILP and $Co_{70}Ru_{30}$@SILP, wherein the rising edge shifts of an additional 0.5 eV to lower energy and a further increase in white-line intensity ~7726 eV is observed. The sample of $Co_{50}Ru_{50}$@SILP submitted for analysis appeared to have undergone a certain degree of adventitious oxidation during handling and its Co K-edge XAS data were not considered further (Figs. 3a, S13).

Little modulation is observed at the Ru K-edge along the Co_xRu_{100-x}@SILP series (Fig. 3b). The large observed broadening is a result of the relatively short 1 s core–hole lifetime of Ru, producing spectra which lack distinguishable features. Based on the similar overlap of these spectra with that of the Ru^0 foil in terms of both edge position and spectral shape, the bulk oxidation state of Ru in the Co_xRu_{100-x}@SILP materials also appears to remain zero-valent (Ru^0).

The Fourier-transform (FT) of the Co K-edge extended X-ray absorption fine structure (EXAFS) region of Co_{100}@SILP exhibits a single, dominating feature at 2.11 Å, along with several long-range features at 3.25, 3.91 and 4.54 Å (Fig. 4a). The addition of 20% Ru to form $Co_{80}Ru_{20}$@SILP results in a significant intensity reduction of the main 2.11 Å feature, along with a contraction to R = 2.08 Å. Additionally, the intensities of the long-range features observed in Co_{100}@SILP are greatly reduced. Increasing Ru content to $Co_{70}Ru_{30}$@SILP results in further intensity reduction of the dominant feature, as well as a further shift to 1.99 Å. This trend continues moving to $Co_{25}Ru_{75}$@SILP, with a large feature peaking at 2.39 Å, with a shoulder at 2.06 Å. The decrease in total FT intensity of the Co EXAFS for all Ru-containing materials relative to Co_{100}@SILP may arise from the presence of additional scattering pathways that result in partial phase-cancellation, and/or increased disorder within the material. The possibility of increased disorder, as previously observed for CoRh nanocrystals and nanoparticles [19,23], is further supported by the disappearance of any clear features in the FT at higher R (3.5–5 Å), which would otherwise arise from ordered long-range single scattering or multi-scattering pathways.

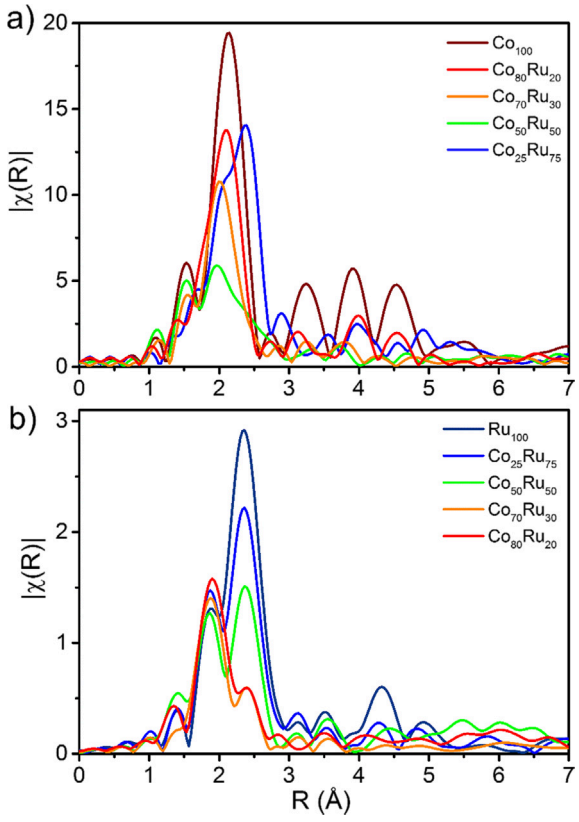

Fig. 4. Comparison of (a) Co K-edge and (b) Ru K-edge EXAFS in R-space (non-phase shift corrected) for Co_xRu_{100-x}@SILP, x = 100, 80, 70, 50, 25, and 0. Spectra were generated by Fourier transform of the k-space from k = 2–13 $Å^{-1}$. EXAFS data were k^3-weighted in the case of Co, and k^2-weighted in the case of Ru.

The Ru K-edge FT-EXAFS exhibit similar trends to those observed for the Co K-edge FT-EXAFS (Fig. 4b). The Ru_{100}@SILP produces a single major feature at 2.36 Å with a shoulder at 1.87 Å, and two minor long-range features at 4.33 and 4.91 Å. Addition of Co to form $Co_{25}Ru_{75}$@SILP results in an overall decreased FT intensity, as well as an increase in intensity of the 1.87 Å feature relative to that at 2.36 Å. Similar to the Co FT-EXAFS, the long-range features at 4.33 and 4.91 Å are significantly reduced in intensity with the addition of Co. This trend continues in $Co_{50}Ru_{50}$@SILP, and further decreasing Ru content to $Co_{70}Ru_{30}$@SILP and $Co_{75}Ru_{25}$@SILP results in a single dominant feature ~1.9 Å, again with a significantly decreased FT intensity (relative to Ru_{100}@SILP).

To further investigate these trends, EXAFS of the Co and Ru K-edge spectra were simultaneously analyzed for a given material composition (detailed in the SI). Over a range of R = 1–3 Å, both Co_{100}@SILP and Ru_{100}@SILP could be reasonably fit using respective single Co-Co and Ru-Ru scattering paths. The Ru K-edge EXAFS of $Co_{80}Ru_{20}$@SILP, $Co_{70}Ru_{30}$@SILP, $Co_{50}Ru_{50}$@SILP and $Co_{25}Ru_{75}$@SILP could also be adequately modeled using Co-Co, Ru-Ru and Ru-Co scattering paths.

EXAFS fitting results are summarized in Tables S3 and S4. A small contraction is observed in the Co-Co distance moving between Co_{100}@SILP and $Co_{80}Ru_{20}$@SILP (~2.48 Å), but expands to 2.53 Å in $Co_{50}Ru_{50}$@SILP and further to 2.55 Å in $Co_{25}Ru_{75}$@SILP. Similarly, the Co-Ru/Ru-Co distance increases from 2.54 Å in $Co_{80}Ru_{20}$@SILP and $Co_{70}Ru_{30}$@SILP to ~2.60 Å in $Co_{50}Ru_{50}$@SILP and $Co_{25}Ru_{75}$@SILP. The fit Ru-Ru distances range between 2.65 and 2.69 Å across the series, appearing slightly contracted in the $Co_{80}Ru_{20}$@SILP and $Co_{70}Ru_{30}$@SILP samples. These fit distances are again consistent with an average zero-valent state of both Co and Ru, and their expansion as a function of increasing Ru content further supports alloying. This is in agreement with our powder X-ray diffraction measurements which show that Co_xRu_{100-x}@SILP materials do not contain free metallic Co (Fig. S16). Atomic distributions were calculated to determine the extent of alloying within the bimetallic nanoparticles. This involves calculation of the parameter *J*, described by Hwang, *et al.*, which relies on the determined degeneracy of the Co-Co, Co-Ru, and Ru-Ru scattering paths [34]. Additionally, we have recently formulated a disorder-corrected atomic distribution parameter, *S*, by modifying the formulation of *J* to include the fit Debye-Waller factors (σ^2) [23]. Fitting results generally support a partially alloyed, homophilic bimetallic structure with bonding affinities in the order Ru-Ru > Co-Co > Co-Ru, based on the determined values of *J* and *S* (Table S3 and Fig. S14). This is similar to the alloying behavior observed in Fe_xRu_{100-x}@SILP nanoparticles, where homophilic structures with respective bond affinities of Ru-Ru > Fe-Fe > Fe-Ru are observed [20].

2.3. Catalysis

The hydrogenation of benzylideneacetone (**1**) was selected as model reaction to investigate the catalytic properties of Fe_xRu_{100-x}@SILP and Co_xRu_{100-x}@SILP materials. Substrate **1** possesses three distinct functional groups such as an aromatic ring, a conjugated double bond (C=C) and a non-benzylic ketone

(C=O), making it a suitable molecular probe to systematically study and compare the reactivity and selectivity of Fe_xRu_{100-x}@SILP and Co_xRu_{100-x}@SILP. Hydrogenation of **1** proceeds through a network of sequential and parallel pathways which can lead to the formation of four different products: 4-phenyl-2-butanone (**1a**), 4-cyclohexyl-2-butanone (**1b**), 4-phenyl-2-butanol (**1c**) and 4-cyclohexyl-2-butanol (**1d**) as depicted in Fig. 5.

Fig. 5a (resp. Fig. 5b) shows the product yield as a function of the Fe:Ru ratio in Fe_xRu_{100-x}@SILP (resp. Co:Ru ratio in Co_xRu_{100-x}@SILP) obtained under an identical set of reaction conditions (T = 150 °C, $p(H_2)$ = 50 bar, t = 16 h, solvent = heptane). The complete datasets are available in the Supporting Information (Tables S5 and S6). Starting with monometallic Ru_{100}@SILP, **1** was fully hydrogenated to give the saturated alcohol **1d** in quantitative yield, which corresponds to the expected reactivity for pure Ru NPs. Incorporation of only a small amount of Fe to produce $Fe_{10}Ru_{90}$ resulted in a sharp switch in selectivity, leading to production of the unsaturated alcohol **1c** in high yield and selectivity (97%, Fig. 5a). The selectivity towards the formation of **1c** was conserved across a range of Fe:Ru ratios, reaching a maximum (>99%) at $Fe_{25}Ru_{75}$. Further increasing the Fe content led to a decrease in total hydrogenation activity, resulting in a mixture of **1a** and **1c** for $Fe_{30}Ru_{70}$. Beyond this point, ketone hydrogenation was not observed anymore, and **1a** was obtained in good yield (82%) using $Fe_{50}Ru_{50}$. Catalysts with even lower Ru contents showed very low activity, possibly due to the oxidation of nanoparticles at high Fe content [20].

When "diluting" Ru with Co instead of Fe, excellent yields of product **1d** could be obtained up to $Co_{25}Ru_{75}$. A sharp switch in selectivity was also observed when further raising the Co content, giving product **1c** in high yield (>99%) across the range $Co_{50}Ru_{50}$ – $Co_{70}Ru_{30}$. Interestingly, a physical mixture of Co_{100}@SILP and Ru_{100}@SILP in a global ratio of $Co_{50}Ru_{50}$ gave **1d** as a major product, outlining the importance of forming the bimetallic M_xRu_{100-x} NPs in a controlled manner (Table S6, Entry 10). A second selectivity switch occurred at $Co_{90}Ru_{10}$, with product **1a** being obtained in high yield (99%) while the C=O hydrogenation activity was suppressed. Selectivity toward the formation of **1a** was conserved up to Co_{100}. While the trends are comparable in both systems, a clear influence of the nature of the 3d metal used on the position of the selectivity switches is evidenced. To gain further insight into catalyst reactivity, time profiles of product formation were recorded using as representative compositions for individual selectivities the materials Ru_{100}@SILP, $Fe_{50}Ru_{50}$@SILP, $Fe_{25}Ru_{75}$@SILP, $Co_{90}Ru_{10}$@SILP, $Co_{70}Ru_{30}$@SILP and $Co_{25}Ru_{75}$@SILP under standard conditions (Fig. 6). A kinetic model based on the Langmuir-Hinshelwood equation was used to analyze the experimental data [35], and the resulting profiles were fitted using the Berkeley Madonna software (see SI for details).

The data generated were used to determine the initial rates for C = C, C = O and arene hydrogenation when applicable (Table 1).

These experiments confirmed the selectivities observed in Fig. 5 for all the catalysts considered. Starting with the selective production of **1a**, $Co_{90}Ru_{10}$@SILP was found to have an initial C=C hydrogenation rate (1.406 $mol \cdot L^{-1} \cdot h^{-1}$) ca. five times higher than $Fe_{50}Ru_{50}$@SILP (0.283 $mol \cdot L^{-1} \cdot h^{-1}$) while containing five times less Ru. With increasing Ru contents in $Fe_{25}Ru_{75}$@SILP and $Co_{70}Ru_{30}$@SILP the C=C hydrogenation became much faster, with full conversion of the substrate in the first hour of reaction (initial C=C hydrogenation rates around 10 $mol \cdot L^{-1} \cdot h^{-1}$ in both cases). Interestingly, this increase in rate does not follow linearly the increase in Ru content. For example when passing from $Fe_{50}Ru_{50}$@SILP to $Fe_{25}Ru_{75}$@SILP, the Ru content was multiplied by 1.5, while the initial C=C hydrogenation rate is multiplied by >30. Such synergistic effect was similarly observed with $Co_{90}Ru_{10}$@SILP and $Co_{70}Ru_{30}$@SILP. In addition, the initial C=O hydrogenation rate was again significantly higher (3x) for $Co_{70}Ru_{30}$@SILP than for $Fe_{25}Ru_{75}$@SILP, despite its much lower (2.5x) Ru content. Using $Co_{25}Ru_{75}$@SILP, the hydrogenation proceeded through intermediates **1a** and **1c** to form **1d** in excellent yield (>99%) after 4 h, with $k_{C=C} > k_{C=O} \gg k_{arene}$. In sharp contrast, Ru_{100}@SILP led to the formation of **1d** through a different pathway involving **1a** and **1b** as intermediates, with $k_{C=C} > k_{arene} \gg k_{C=O}$. A similar "pathway switch" was previously reported for bimetallic CoRh catalysts [23]. Interestingly, $Co_{25}Ru_{75}$@SILP led to a comparable productivity of fully saturated product **1d** as Ru_{100}@SILP, while containing 25% less Ru. Three main points can be extracted from the present results: (1) the position of the selectivity switches as a function of the M:Ru ratios strongly

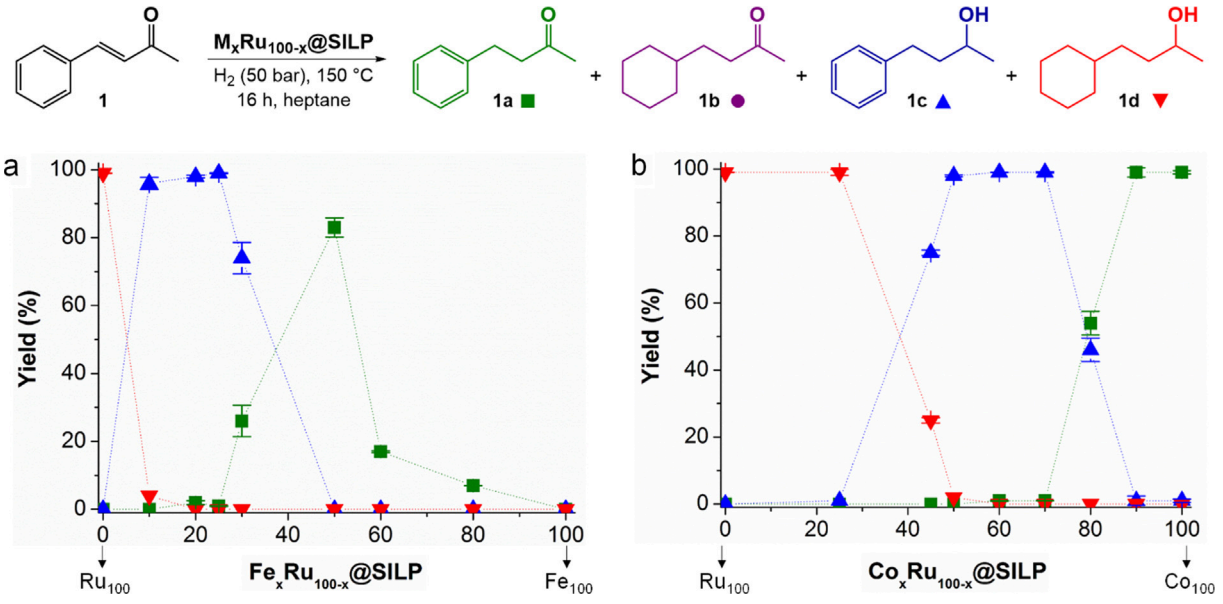

Fig. 5. Hydrogenation of benzylideneacetone using a series of (a) Fe_xRu_{100-x}@SILP and (b) Co_xRu_{100-x}@SILP catalysts with different M:Ru ratios. Reaction conditions: Catalyst (20.0 mg, 0.008 mmol [M]), 18 h, 150 °C, H_2 (50 bar at r.t.), benzylideneacetone (117 mg, 0.8 mmol, 100 eq.), n-heptane (0.5 mL). Yield is determined by GC-FID using tetradecane as an internal standard.

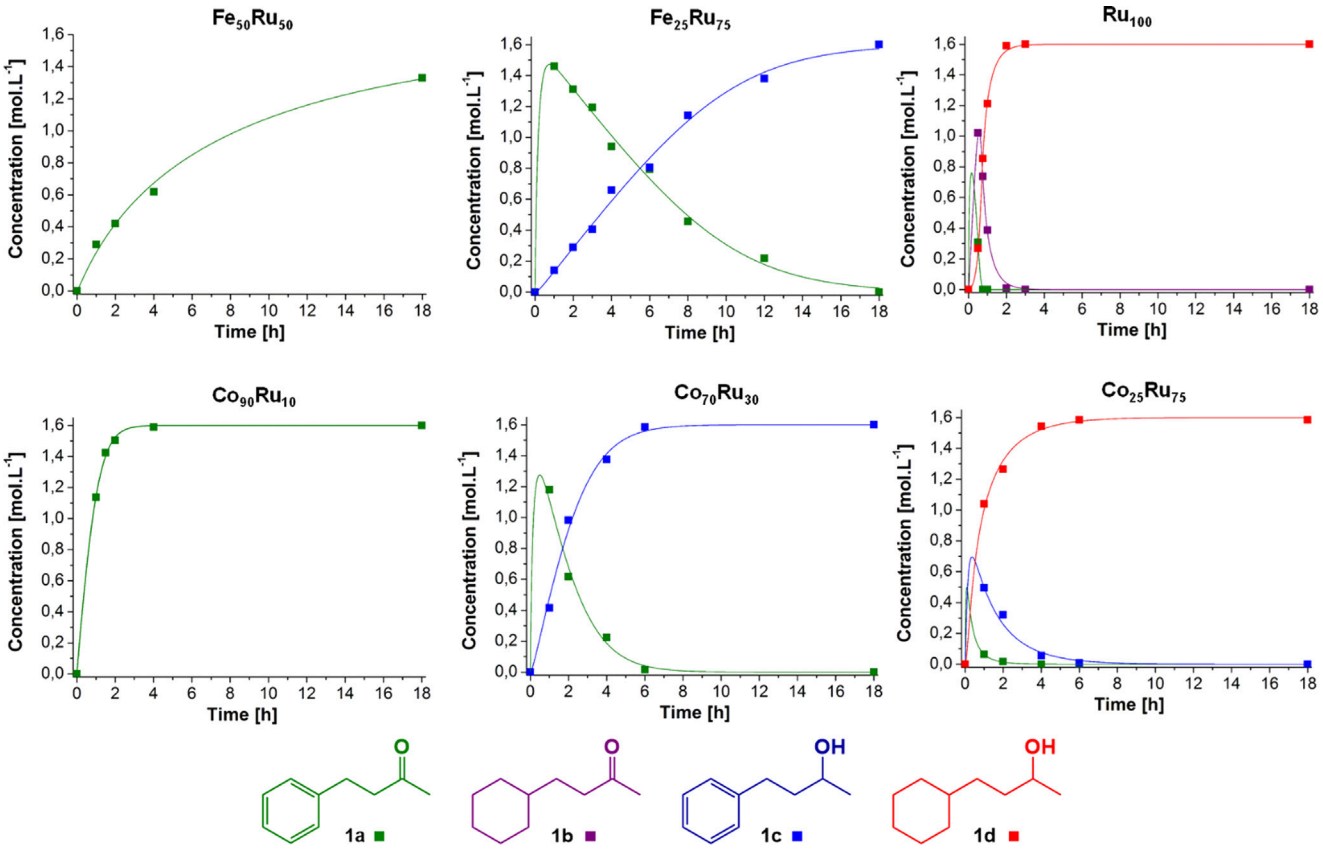

Fig. 6. Time profiles recorded using (a) $Fe_{50}Ru_{50}$@SILP, (b) $Fe_{25}Ru_{75}$@SILP, (c) Ru_{100}@SILP, (d) $Co_{90}Ru_{10}$@SILP, (e) $Co_{70}Ru_{30}$@SILP, (f) $Co_{25}Ru_{75}$@SILP. Reaction conditions: Cat. (20.0 mg, 0.008 mmol [M]), H_2 (50 bar), benzylideneacetone (117 mg, 0.80 mmol, 100 eq.), 150 °C, n-heptane (0.5 mL). Yield determined by GC-FID using tetradecane as internal standard. See Tables S7–S12 for complete data set. Experimental data fitted using Berkley Madonna (see SI for details). Solid lines are the values predicted by the model. Solid points are the experimental data.

Table 1
Initial C=C, C=O, and aromatic ring hydrogenation rates of M_xRu_{100-x}@SILP catalysts.

Catalyst	Initial hydrogenation rates ($mol \cdot L^{-1} \cdot h^{-1}$)		
	$k^0_{C=C}$	$k^0_{C=O}$	k^0_{arene}
$Fe_{50}Ru_{50}$	0.283	–	–
$Fe_{25}Ru_{75}$	9.427	0.154	–
$Co_{90}Ru_{10}$	1.406	–	–
$Co_{70}Ru_{30}$	10.682	0.498	–
$Co_{25}Ru_{75}$	16.655	4.077	1.229
Ru_{100}	21.559	1.251	2.379

Reaction conditions: Cat. (20.0 mg, 0.008 mmol [M]), H_2 (50 bar), benzylideneacetone (117 mg, 0.80 mmol, 100 eq.), 150 °C, n-heptane (0.5 mL). Yield determined by GC-FID using tetradecane as internal standard.

depends on the nature of the 3d metal used to "dilute" Ru; (2) to reach a given selectivity, CoRu catalysts systematically require less Ru while being significantly more active than FeRu catalysts; (3) the hydrogenation sequence of the functional groups is different in bimetallic FeRu and CoRu catalysts ($k_{C=O} \gg k_{arene}$) as compared to monometallic Ru catalysts ($k_{arene} \gg k_{C=O}$).

The enhanced C=O hydrogenation rates observed with $Co_{25}Ru_{75}$ in comparison with Ru_{100} can be rationalized by a more polarized activation of H_2 coupled to a facilitated activation of the C=O bond on the oxophilic surface. Above specific Fe and Co contents, aromatic hydrogenation is suppressed due to the absence of suitable Ru ensembles. The in-depth characterization of FeRu and CoRu NPs showed bimetallic alloy-type NPs with metals in the formal oxidation state zero, without significant difference in structural or electronic (Ru) properties. The strong dependency on the nature of the 3d metal used may partially originate from the fact that Co possesses an intrinsically better hydrogenation activity than Fe. In addition, it can be tentatively attributed to a dynamic modification of FeRu and CoRu NPs surface composition under reaction conditions, similar to what has been previously proposed in the case of CoRh@SILP catalysts [23], and evidenced for CuPd [36] and CoPd [37] alloys. The oxophilic Fe and Co atoms may indeed be attracted by the polar substrate during the reaction, resulting in an enrichment of the alloys' surfaces in 3d metal.

To investigate this hypothesis, a short series of Co_xRu_{100-x}@SILP catalysts ($Co_{90}Ru_{10}$, $Co_{80}Ru_{20}$, $Co_{50}Ru_{50}$) was used to hydrogenate styrene (**2**) as non-oxygenated substrate under standard conditions (Table S13). $Co_{90}Ru_{10}$@SILP and $Co_{80}Ru_{20}$@SILP produced ethylbenzene (**2a**) in quantitative yields, with a selectivity similar to what was observed previously with benzylideneacetone (Fig. 5). In contrast, the use of $Co_{50}Ru_{50}$@SILP gave ethylcyclohexane as major product (88% yield), while the same catalyst was found inactive toward aromatic hydrogenation in the case of benzylideneacetone. A similar observation was performed with $Fe_{10}Ru_{90}$@SILP (Table S13). These results indicate that the position of the selectivity switch can shift depending on the substrate properties, strongly supporting a dynamic modification of the bimetallic NPs surface composition assisted by benzylideneacetone. On this basis, one could expect the more oxophilic Fe atoms to be even more strongly attracted than the Co atoms [38], leading to different Fe:Ru and Co:Ru ratios at the NPs surface even when starting from an identical M:Ru global ratio. This could possibly explain why the position of the selectivity switches is different in both systems, with much less Fe than Co needed to change the activity and selectivity of the

M_xRu_{100-x} alloys, and in particular to suppress aromatic ring hydrogenation (Fe_{10} versus Co_{50}). While our catalytic data are supportive of this hypothesis, its rigorous investigation by characterization of the catalysts under dynamic conditions using operando X-Ray spectroscopies is underway and will be the subject of future reports.

3. Conclusions

In conclusion, we report a versatile organometallic approach for the preparation of bimetallic FeRu and CoRu nanoparticles of precisely controlled composition on an imidazolium-based supported ionic liquid phase. The resulting Fe_xRu_{100-x}@SILP and Co_xRu_{100-x}@SILP materials were characterized using a combination of techniques including electron microscopy, powder XRD and XAS, evidencing the formation of small (1–4 nm), well-dispersed, alloyed nanoparticles in a zero-valent state. The catalytic properties of Fe_xRu_{100-x}@SILP and Co_xRu_{100-x}@SILP in hydrogenation were systematically investigated using benzilideneacetone as molecular probe. While the substrate was fully hydrogenated following pathway **1** => **1a** => **1b** => **1d** using monometallic Ru_{100}@SILP, introducing even very small quantities of Fe or Co led to a clear modification of the hydrogenation pathway to **1** => **1a** => **1c** (=> **1d**). In addition, progressively increasing the content of Fe and Co in FeRu and CoRu NPs led to selectivity switches, with first the suppression of the arene hydrogenation (ratios [$Fe_{10}Ru_{90}$ – $Fe_{25}Ru_{75}$] and [$Co_{50}Ru_{50}$-$Co_{25}Ru_{75}$], respectively). This reactivity was associated with an increase in C=O hydrogenation activity as compared to monometallic Ru_{100}@SILP, evidencing strong synergistic effects. Further increasing the Fe or Co content ultimately led to the suppression of the C=O hydrogenation as well. While the selectivity switch patterns are similar for Fe_xRu_{100-x}@SILP and Co_xRu_{100-x}@SILP catalysts, the positions of the switches and the amplitude of the synergistic effects appear strongly dependent on the nature of the 3d metal used for the "dilution" of Ru. In particular, Co_xRu_{100-x}@SILP catalysts are significantly more reactive to reach a given selectivity at a systematically higher content of the 3d metal as compared to the Fe_xRu_{100-x}@SILP catalysts. This effect is tentatively attributed to an interplay of intrinsic differences in the hydrogenation capabilities of Fe and Co and substrate-induced dynamic modifications of the NPs surface composition under catalytic conditions due to the different oxophilicity of Fe and Co.

Overall, the results presented here show how the preparation of well-defined and tunable supported bimetallic NPs can provide fine control over activity and selectivity in hydrogenation. This approach is versatile and can potentially be extended to other combinations of metals, paving the way toward the development of tailor-made bimetallic catalytic systems which allow for the precise adjustment of H_2 activation, H_2 activation mode, and substrate activation.

Declaration of Competing Interest

The authors declare that they have no known competing financial interests or personal relationships that could have appeared to influence the work reported in this paper.

Acknowledgement

The authors acknowledge financial support by the Max Planck Society and by the Deutsche Forschungsgemeinschaft (DFG, German Research Foundation) under Germany's Excellence Strategy – Exzellenzcluster 2186 „The Fuel Science Center" ID: 390919832. The authors would like to thank, Norbert Pfänder (Max Planck Institute for Chemical Energy Conversion) and Silvia palm (Max-Planck-Institut für Kohlenforschung) for STEM/EDX and SEM/EDX analysis. The authors are also thankful to Annika Gurowski, Alina Jakubowski, and Justus Werkmeister (MPI-CEC) for GC and GC-MS measurements. We acknowledge DESY (Hamburg, Germany), a member of the Helmholtz Association HGF, for the provision of experimental facilities. For parts of this research carried out at PETRA III, we would like to thank Dr. Edmund Welter for assistance in using beamline P65.

Appendix A. Supplementary material

Supplementary data to this article can be found online at https://doi.org/10.1016/j.jcat.2022.01.030.

References

[1] L. Liu, A. Corma, Metal catalysts for heterogeneous catalysis: from single atoms to nanoclusters and nanoparticles, Chem. Rev. 118 (2018) 4981–5079.
[2] L. Zhang, M. Zhou, A. Wang, T. Zhang, Selective hydrogenation over supported metal catalysts: from nanoparticles to single atoms, Chem. Rev. 120 (2020) 683–733.
[3] T. Mitsudome, Y. Mikami, M. Matoba, T. Mizugaki, K. Jitsukawa, K. Kaneda, Design of a silver-cerium dioxide core-shell nanocomposite catalyst for chemoselective reduction reactions, Angew. Chem., Int. Ed. 51 (2012) 136–139.
[4] J. Harris, S. Andersson, H_2 dissociation at metal surfaces, Phys. Rev. Lett. 55 (1985) 1583–1586.
[5] A. Bordet, W. Leitner, Metal nanoparticles immobilized on molecularly modified surfaces: versatile catalytic systems for controlled hydrogenation and hydrogenolysis, Acc. Chem. Res. 54 (9) (2021) 2144–2157.
[6] C. Fan, Y.-A. Zhu, X.-G. Zhou, Z.-P. Liu, Catalytic hydrogenation of benzene to cyclohexene on Ru(0001) from density functional theory investigations, Catal. Today 160 (2011) 234.
[7] A. Fedorov, H.-J. Liu, H.-K. Lo, C. Copéret, Silica-supported Cu nanoparticle catalysts for alkyne semihydrogenation: effect of ligands on rates and selectivity, J. Am. Chem. Soc. 138 (50) (2016) 16502–16507.
[8] I. Schrader, J. Warneke, J. Backenköhler, S. Kunz, Functionalization of platinum nanoparticles with L-proline: simultaneous enhancements of catalytic activity and selectivity, J. Am. Chem. Soc. 137 (2015) 905–912.
[9] J.B. Ernst, S. Muratsugu, F. Wang, M. Tada, F. Glorius, Tunable heterogeneous catalysis: N-heterocyclic carbenes as ligands for supported heterogeneous Ru/K-Al_2O_3 catalysts to tune reactivity and selectivity, J. Am. Chem. Soc. 138 (34) (2016) 10718–10721.
[10] S. Yun, S. Lee, S. Yook, H.A. Patel, C.T. Yavuz, M. Choi, Cross-linked, "Poisonous" polymer: thermochemically stable catalyst support for tuning chemoselectivity, ACS Catal. 6 (2016) 2435–2442.
[11] A. Cooper, B. Bachiller-Baeza, J.A. Anderson, I. Rodriguez-Ramos, A. Guerrero-Ruiz, Design of surface sites for the selective hydrogenation of 1,3-butadiene on Pd nanoparticles: Cu bimetallic formation and sulfur poisoning, Cat. Sci. Tech. 4 (2014) 1446–1455.
[12] A. Bordet, S. El Sayed, M. Sanger, K.J. Boniface, D. Kalsi, K.L. Luska, P.G. Jessop, W. Leitner, Selectivity control in hydrogenation through adaptive catalysis using ruthenium nanoparticles on a CO_2-responsive support, Nat. Chem. 13 (2021) 916–922.
[13] L. Ye, H. Lin, H. Zhou, Y. Yuan, Support and size effects of ruthenium catalysts with a chiral modifier for asymmetric hydrogenation of aromatic ketones, J. Phys. Chem. C 114 (46) (2010) 19752–19760.
[14] A. Bordet, G. Moos, C. Welsh, P. Licence, K.L. Luska, W. Leitner, Molecular control of the catalytic properties of rhodium nanoparticles in Supported Ionic Liquid Phase (SILP) systems, ACS Catal. 10 (2020) 13904–13912.
[15] M. Sankar, N. Dimitratos, P.J. Miedziak, P.P. Wells, C.J. Kiely, G.J. Hutchings, Designing bimetallic catalysts for a green and sustainable future, Chem. Soc. Rev. 41 (2012) 8099.
[16] J. Lee, Y.T. Kim, G.W. Huber, Aqueous-phase hydrogenation and hydrodeoxygenation of biomass-derived oxygenates with bimetallic catalysts, Green Chem. 16 (2014) 708.
[17] D.M. Alonso, S.G. Wettstein, J.A. Dumesic, Bimetallic catalysts for upgrading of biomass to fuels and chemicals, Chem. Soc. Rev. 41 (2012) 8075.
[18] A. Wong, Q. Liu, S. Griffin, A. Nicholls, J.R. Regalbuto, Synthesis of ultrasmall, homogeneously alloyed, bimetallic nanoparticles on silica supports, Science 358 (6369) (2017) 1427–1430.
[19] K. Ding, D.A. Cullen, L. Zhang, Z. Cao, A.D. Roy, I.N. Ivanov, D. Cao, A General synthesis approach for supported bimetallic nanoparticles via surface inorganometallic chemistry, Science 362 (6414) (2018) 560–564.
[20] K.L. Luska, A. Bordet, S. Tricard, I. Sinev, W. Grünert, B. Chaudret, W. Leitner, Enhancing the catalytic properties of ruthenium nanoparticle-SILP catalysts by dilution with iron, ACS Catal. 6 (2016) 3719–3726.
[21] L. Offner-Marko, A. Bordet, G. Moos, S. Tricard, S. Rengshausen, B. Chaudret, K. L. Luska, W. Leitner, Bimetallic nanoparticles in supported ionic liquid phases as multifunctional catalysts for the selective hydrodeoxygenation of aromatic substrates, Angew. Chem. Int. Ed. 57 (2018) 12721–12726.

[22] L. Goclik, L. Offner-Marko, A. Bordet, W. Leitner, Selective hydrodeoxygenation of hydroxyacetophenones to ethyl-substituted phenol derivatives using a FeRu@SILP catalyst, Chem. Comm. 56 (2020) 9509–9512.
[23] S. Rengshausen, C. Van Stappen, N. Levin, S. Tricard, K.L. Luska, S. DeBeer, B. Chaudret, A. Bordet, W. Leitner, Organometallic synthesis of bimetallic cobalt-rhodium nanoparticles in supported ionic liquid phases (Co_xRh_{100-x}@SILP) as catalysts for the selective hydrogenation of multifunctional aromatic substrates, Small 17 (5) (2021) 2006683, https://doi.org/10.1002/smll.v17.510.1002/smll.202006683.
[24] V. Kelsen, A. Meffre, P.-F. Fazzini, P. Lecante, B. Chaudret, How to modulate catalytic properties in nanosystems: the case of iron-ruthenium nanoparticles, ChemCatChem 6 (6) (2014) 1714–1720.
[25] A. Meffre, V. Iablokov, Y. Xiang, R. Barbosa, P.-F. Fazzini, V. Kelsen, N. Kruse, B. Chaudret, Influence of chemical composition on the catalytic activity of small bimetallic FeRu nanoparticles for fischer-tropsch syntheses, Catal. Lett. 145 (2015) 373–379.
[26] M.I. Qadir, A. Weilhard, J.A. Fernandes, I. de Pedro, B.J.C. Vieira, J.C. Waerenborgh, J. Dupont, Selective carbon dioxide hydrogenation driven by ferromagnetic RuFe nanoparticles in ionic liquids, ACS Catal. 8 (2018) 1621–1627.
[27] Y. Jin, F. Chen, J. Wang, Achieving low charge overpotential in a Li-CO2 battery with bimetallic RuCo nanoalloy decorated carbon nanofiber cathodes, ACS. Sust. Chem. Eng. 8 (2020) 2783–2792.
[28] F. Zhang, Y. Zhu, Y.u. Chen, Y. Lu, Q. Lin, L. Zhang, S. Tao, X. Zhang, H. Wang, RuCo alloy bimodal nanoparticles embedded in N-doped carbon: a superior ph-universal electrocatalyst outperforms benchmark pt for the hydrogen evolution reaction, J. Mater. Chem. A 8 (25) (2020) 12810–12820.
[29] H. Wang, Y. Yang, F.J. DiSalvo, H.D. Abruña, Multifunctional electrocatalysts: Ru−M (M = Co, Ni, Fe) for alkaline fuel cells and electrolyzers, ACS Catal. 10 (2020) 4608–4616.
[30] C. Menghuan, L. Zhou, L.u. Di, L.i. Yue, N. Honghui, P. Yaxi, X.u. Hongkun, P. Weiwei, Z. Shuren, RuCo bimetallic alloy nanoparticles immobilized on multi-porous MIL-53(Al) as a highly efficient catalyst for the hydrolytic reaction of ammonia borane, Int. J. Hydrog. Energy 43 (3) (2018) 1439–1450.
[31] B. Sen, S. Kuzu, E. Demir, S. Akocak, F. Sen, Highly monodisperse RuCo nanoparticles decorated on functionalized multiwalled carbon nanotube with the highest observed catalytic activity in the dehydrogenation of dimethylamine-borane, Int. J. Hydrog. Energy 42 (36) (2017) 23292–23298.
[32] Y. Wang, T. Gao, Y. Lu, Y. Wang, Q. Cao, W. Fang, Efficient Hydrogenation of Furfural to Furfuryl Alcohol by Magnetically Recoverable RuCo Bimetallic Catalyst, Green Energ Envir, 2020, in press.
[33] M. Esen, S. Akmaz, S.N. Koç, M.A. Gürkaynak, The hydrogenation of 5-hydroxymethylfurfural (HMF) to 2,5-himethylfuran (DMF) with sol-gel Ru-Co/SiO_2 catalyst, J. Sol-Gel Sci. Technol. 91 (2019) 664–672.
[34] B.-J. Hwang, L.S. Sarma, J.-M. Chen, C.-H. Chen, S.-C. Shih, G.-R. Wang, D.-G. Liu, J.-F. Lee, M.-T. Tang, Structural models and atomic distribution of bimetallic nanoparticles as investigated by X-ray absorption spectroscopy, J. Am. Chem. Soc. 127 (31) (2005) 11140–11145.
[35] S.L. Kiperman, Some problems of chemical kinetics in heterogeneous hydrogenation catalysis, Stud. Surf. Sci. Catal. 27 (1986) 1–52.
[36] J.S. Bradley, E.W. Hill, B. Chaudret, A. Duteil, Surface chemistry on colloidal metals. reversible adsorbate-induced surface composition changes in colloidal palladium-copper alloys, Langmuir 11 (3) (1995) 693–695.
[37] C.H. Wu, C. Liu, D. Su, H.L. Xin, H.-T. Fang, B. Eren, S. Zhang, C.B. Murray, M.B. Salmeron, Bimetallic synergy in cobalt-palladium nanocatalysts for CO oxidation, Nat. Catal. 2 (2019) 78–85.
[38] Z. Jiang, W. Wan, Z. Lin, J. Xie, J.G. Chen, Understanding the role of M/Pt(111) (M = Fe Co, Ni, Cu) bimetallic surfaces for selective hydrodeoxygenation of furfural, ACS Catal. 7 (2017) 5758–5765.